




Article

# Tunable Electronic and Magnetic Properties of 3d Transition Metal Atom-Intercalated Transition Metal Dichalcogenides: A Density Functional Theory Study

Yujie Liu <sup>1</sup>, Guang Yang <sup>1</sup>, Zhiwen He <sup>1</sup>, Yanbiao Wang <sup>2,\*</sup>, Xianghong Niu <sup>3,\*</sup> , Sake Wang <sup>4</sup> , Yongjun Liu <sup>1</sup> and Xiuyun Zhang <sup>1</sup> 

<sup>1</sup> College of Physics Science and Technology, Yangzhou University, Yangzhou 225002, China; 2127012228@stu.yzu.edu.cn (Y.L.); yguang@gs.zzu.edu.cn (G.Y.); 220903214@stu.yzu.edu.cn (Z.H.); yjliu@yzu.edu.cn (Y.L.); xyzhang@yzu.edu.cn (X.Z.)

<sup>2</sup> Department of Fundamental Courses, Wuxi Institute of Technology, Wuxi 214121, China

<sup>3</sup> Institute of Advanced Materials (IAM), College of Electronic and Optical Engineering, School of Science, Nanjing University of Posts & Telecommunications, Nanjing 210023, China

<sup>4</sup> College of Science, Jinling Institute of Technology, 99 Hongjing Avenue, Nanjing 211169, China; isaacwang@jit.edu.cn

\* Correspondence: wangyb@wxit.edu.cn (Y.W.); xhniu@njupt.edu.cn (X.N.)

**Abstract:** Currently, intercalation has become an effective way to modify the fundamental properties of two-dimensional (2D) van der Waals (vdW) materials. Using density functional theory, we systematically investigated the structures and electronic and magnetic properties of bilayer transition metal dichalcogenides (TMDs) intercalated with 3d TM atoms (TM = Sc–Ni), TM@BL\_MS<sub>2</sub> (M = Mo, V). Our results demonstrate that all the studied TM@BL\_MS<sub>2</sub>s are of high stability, with large binding energies and high diffusion barriers of TM atoms. Interestingly, most TM@BL\_MoS<sub>2</sub>s and TM@BL\_VS<sub>2</sub>s are found to be stable ferromagnets. Among them, TM@BL\_MoS<sub>2</sub>s (TM = Sc, Ti, Fe, Co) are ferromagnetic metals, TM@BL\_MoS<sub>2</sub> (TM = V, Cr) and TM@BL\_VS<sub>2</sub> (TM = Sc, V) are ferromagnetic half-metals, and the remaining systems are found to be ferromagnetic semiconductors. Exceptions are found for Ni@BL\_MoS<sub>2</sub> and Cr@BL\_VS<sub>2</sub>, which are nonmagnetic semiconductors and ferrimagnetic half-metals, respectively. Further investigations reveal that the electromagnetic properties of TM@BL\_MoS<sub>2</sub> are significantly influenced by the concentration of intercalated TM atoms. Our study demonstrates that TM atom intercalation is an effective approach for manipulating the electromagnetic properties of two-dimensional materials, facilitating their potential applications in spintronic devices.

**Keywords:** intercalation; transition metal; transition metal dichalcogenides; ferromagnetic; first-principles calculations



**Citation:** Liu, Y.; Yang, G.; He, Z.; Wang, Y.; Niu, X.; Wang, S.; Liu, Y.; Zhang, X. Tunable Electronic and Magnetic Properties of 3d Transition Metal Atom-Intercalated Transition Metal Dichalcogenides: A Density Functional Theory Study. *Inorganics* **2024**, *12*, 237. <https://doi.org/10.3390/inorganics12090237>

Academic Editor: Jean Pierre Djukic

Received: 1 August 2024

Revised: 24 August 2024

Accepted: 27 August 2024

Published: 29 August 2024



**Copyright:** © 2024 by the authors. Licensee MDPI, Basel, Switzerland. This article is an open access article distributed under the terms and conditions of the Creative Commons Attribution (CC BY) license (<https://creativecommons.org/licenses/by/4.0/>).

## 1. Introduction

Since the discovery of graphene [1,2], various two-dimensional (2D) materials with finite thickness have attracted wide attention due to their versatile properties and potential applications in various fields [3,4]. Particularly, the 2D candidates with rich magnetic properties are regarded as a good platform for the development of spintronic devices [2–6], which facilitates low energy consumption and fast device operation. Experimentally, a few 2D magnetic materials have been produced, including ferromagnetic (FM) transition metal trihalide monolayer (e.g., CrI<sub>3</sub>, VI<sub>3</sub>) [7,8], Cr<sub>2</sub>Ge<sub>2</sub>Te<sub>6</sub> monolayer [9], Fe<sub>3</sub>GeTe<sub>2</sub> monolayer [10], and antiferromagnetic (AFM) MnPS<sub>3</sub> monolayer [11–13]. Inspired by the above progress, considerable theoretical efforts have been made on the development of 2D magnetic candidates, such as transition metal (TM) borides [14–16], TM phosphides [17–19], TM disulfides [20–22], etc.

Despite the theoretical and experimental achievements, the members of known 2D FM or antiferromagnetic (AFM) candidates are still limited. Moreover, to advance the development of 2D spintronics devices, two major challenges should be solved: (i) robust magnetic orders with high transition temperature and (ii) the feasibility of fabrication experimentally, for example, many predicted 2D FM or antiferromagnetic (AFM) candidates so far face challenges in preparation. Therefore, finding a feasible way to obtain 2D magnetic materials is still a great challenge. It is found that introducing magnetism to grown non-magnetic 2D materials is an effective way to solve the challenge (ii) mentioned above. Various modification strategies have been developed for nonmagnetic materials in terms of tuning their electronic and magnetic properties, such as atom doping or substitution [23], introducing vacancies [24], external strains [25], etc. Unfortunately, these methods usually bring significant distortion to the structures.

Alternatively, the intercalation of magnetic species into the vdW gap of 2D materials provides a promising way to explore novel 2D magnets without destroying the host lattices [26–30]. Taking 2D transition-metal dichalcogenides (TMDs) as an example, the TM atom-intercalated vdW TMDs with different stoichiometries have been produced by electrochemical intercalations, which has been identified to be an effective way to modulate the electronic and magnetic properties [31,32]. For example, Guzman et al. presented a comprehensive investigation into the structural evolution of CVD-grown  $V_{1+x}Se_2$  nanoplates. They found the  $VSe_2$ -to- $V_5Se_8$  phase and  $V_3Se_4$ -to- $V_5Se_8$  structural transformation under 300 °C and 250 °C annealing [33]. Zhao et al. extended the ferromagnetic order in tantalum-intercalated  $TaS(Se)_y$ , such as  $Ta_9S_{16}$ ,  $Ta_7S_{12}$ ,  $Ta_{10}S_{16}$ , and  $Ta_8Se_{12}$  [34]. Besides, FM orders were observed in ultra-thin films of  $V_5X_8$  ( $X = S, Se$ ) [35] and  $V_5Se_8/NbSe_2$  2D-heterostructures [36]. In addition, a number of different  $Cr_{1+\delta}Te_2$  phases were found to have a broad range of magnetic orders and novel magnetic phases [37,38]. Using density functional theory calculation, Kumar et al. found that the late TM-intercalated  $WSe_2$  exhibited substantial magnetic moments and pronounced ferromagnetic order [27]. Guo et al. found that filling either Cr or I atoms into the van der Waals gap of stacked and twisted  $CrI_3$  bilayers can induce the double exchange effect and significantly strengthen the interlayer ferromagnetic coupling [39]. Correspondence to the experimental progress, the theoretical understanding of the electronic and magnetic properties of these intercalated systems is still very limited.

In this work, by using the density functional theory, we systematically studied the structural, electronic, and magnetic properties of 3d TM atom-intercalated bilayers  $MS_2$  ( $M = Mo, V$ ),  $TM@BL\_MS_2$  ( $TM = Sc-Ni$ ). Our results show that all the systems are very stable with large binding energies. Except for  $Ni@BL\_MoS_2$  and  $Cr@BL\_VS_2$ , all the other  $TM@BL\_MoS_2$ s and  $TM@BL\_VS_2$ s are ferromagnetic (half-)metals and semiconductors.  $Ni@BL\_MoS_2$  is a nonmagnetic semiconductor, and  $Cr@BL\_VS_2$  is a ferrimagnetic half-metal. Most importantly, the electronic and magnetic properties of these  $TM@BL\_MoS_2$ s are largely influenced by the concentration of TM atoms.

## 2. Results and Discussion

### 2.1. Structure and Stability of $TM@BL\_MS_2$ ( $TM = Sc-Ni, M = Mo, V$ )

The space groups for H- $MoS_2$  and H- $VS_2$  monolayers are the same,  $P\bar{6}m2$ , with lattice constants of 3.16 Å and 3.17 Å, respectively. The  $MoS_2$  monolayer is a nonmagnetic semiconductor [40–42], and the H- $VS_2$  monolayer is predicted to be a FM semiconductor with a magnetic moment of 1.0  $\mu_B$  per V atom [43–47]. Three types of stacking configurations were considered for  $MoS_2$  or  $VS_2$  bilayers: (i) AA-stacking, in which the atoms from the top  $MS_2$  layer sit exactly atop those in the bottom layer [see Figures 1a,f and S1a,f]; (ii) AB-stacking, where both layers rotate by 30 degrees relative to each other, with the M atoms from the top layer sitting atop those in the bottom layer, and the S atoms from one layer located on the hexagonal hole site of the adjacent layer [see Figures 1b,g and S1b,g]; (iii) AB'-stacking, which is similar to AB-stacking but with reversed interlayer configurations of the M/S atoms [see Figures 1c,h and S1c,h]. Our results show that the

favored stacking structures for bilayer MoS<sub>2</sub> and VS<sub>2</sub> are the AB-stacking ones, which are 0.60 eV/0.56 eV and 0.55 eV/0.55 eV lower in energy than their AA- and AB'-stacking counterparts, respectively. In the following study, we only focus on the AB-stacked MoS<sub>2</sub> bilayer and VS<sub>2</sub> bilayer, whose interlayer spacing is 3.19 Å and 3.04 Å, respectively. In order to study the most stable configurations of TM@BL\_Mo(V)S<sub>2</sub>s, two configurations with different intercalation sites for TM atoms are considered: (i) Conf\_I: in which the intercalated TM atom sits below the Mo/V atom (A site) in the top layer of Mo(V)S<sub>2</sub> [see Figure 1d,i and Figure S1d,i]; (ii) Conf\_II: in which the TM atom is located below the S atom (B site) of the upper layer of Mo(V)S<sub>2</sub> [see Figures 1e,j and S1e,j]. Testing calculations show that the TM@BL\_MoS<sub>2</sub>s with Conf\_I intercalation are the favored ones, which are 1.3 eV and 0.9 eV lower than that with B Site intercalating for Ti@BL\_MoS<sub>2</sub> and V@BL\_MoS<sub>2</sub>, respectively. Therefore, we will only use Conf\_I for further exploration, and the optimized structures are shown in Figure 2 and Figure S2 in the Supporting Information (SI). The detailed structural information is summarized in Table 1.

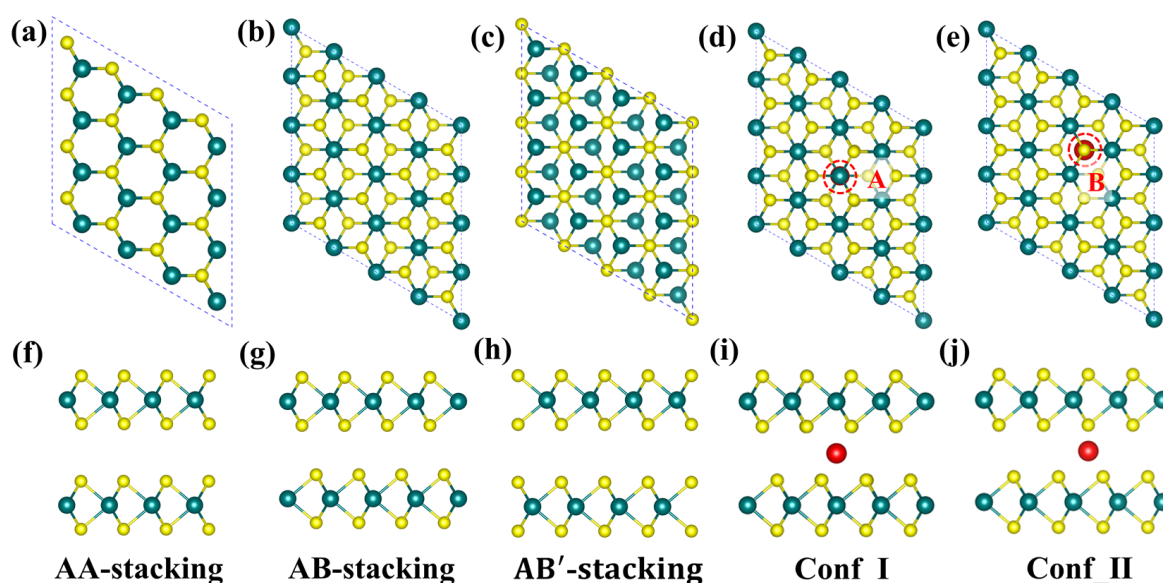


**Figure 1.** Top and side views of (a,f) AA-, (b,g) AB-, and (c,h) AB'- stacking of bilayer MoS<sub>2</sub>. Top and side views of TM@BL\_MoS<sub>2</sub> with TM intercalating in the (d,i) A site and (e,j) B site.

Except for Ni@BL\_MoS<sub>2</sub>, all the TM atoms prefer to occupy the center of the vertical interlayer space of both TM@BL\_MoS<sub>2</sub>s and TM@BL\_VS<sub>2</sub>s (see Figures 2 and S2), in which the TM atoms are distanced from the two-side MS<sub>2</sub> layer by about 1.09 Å~1.73 Å and 1.50 Å~1.69 Å for TM@BL\_MoS<sub>2</sub>s and TM@BL\_VS<sub>2</sub>s, respectively. Compared with free-standing Mo(V)S<sub>2</sub> bilayers, the intercalation of TM atoms enlarges the interlayer spacing to 3.16 Å~3.46 Å and 3.05 Å~3.37 Å in the case of TM@BL\_MoS<sub>2</sub>s and TM@BL\_VS<sub>2</sub>s, respectively (see Table 1). To quantitatively characterize the structural stability of these TM@BL\_Mo(V)S<sub>2</sub> systems, we calculate the binding energies ( $E_b$ s) of the TM atom to the Mo(V)S<sub>2</sub> bilayers based on the following equation:

$$E_b = E_{\text{Total}} - E_{\text{TM}} - 2E_{\text{MS}_2} \quad (1)$$

where  $E_{\text{Total}}$ ,  $E_{\text{TM}}$ , and  $E_{\text{MS}_2}$  represent the total energy of the TM@BL\_MS<sub>2</sub>, the isolated transition metal atom, and the free-standing Mo(V)S<sub>2</sub> bilayers, respectively. As shown in Table 1 and Figure 3a, the calculated  $E_b$ s are around -7.21~-5.19 eV and -6.69~-4.23 eV for TM@BL\_MoS<sub>2</sub>s and TM@BL\_VS<sub>2</sub>s, respectively, which are comparable to those of TM-intercalated graphene/TMD heterostructures [48]. Such large negative  $E_b$  values indicate that the intercalation of TM atom in Mo(V)S<sub>2</sub> bilayers is energetically favorable. In the case of TM@BL\_MoS<sub>2</sub>, the  $E_b$  of Ni@BL\_MoS<sub>2</sub> system is the lowest (-7.21 eV),

and that of Ti@BL\_MoS<sub>2</sub> is the highest (−5.19 eV). For the TM@BL\_VS<sub>2</sub> system, the  $E_b$  of Ti intercalation system is the lowest (−6.69 eV), and that of Cr intercalation system is the highest (−4.23 eV).

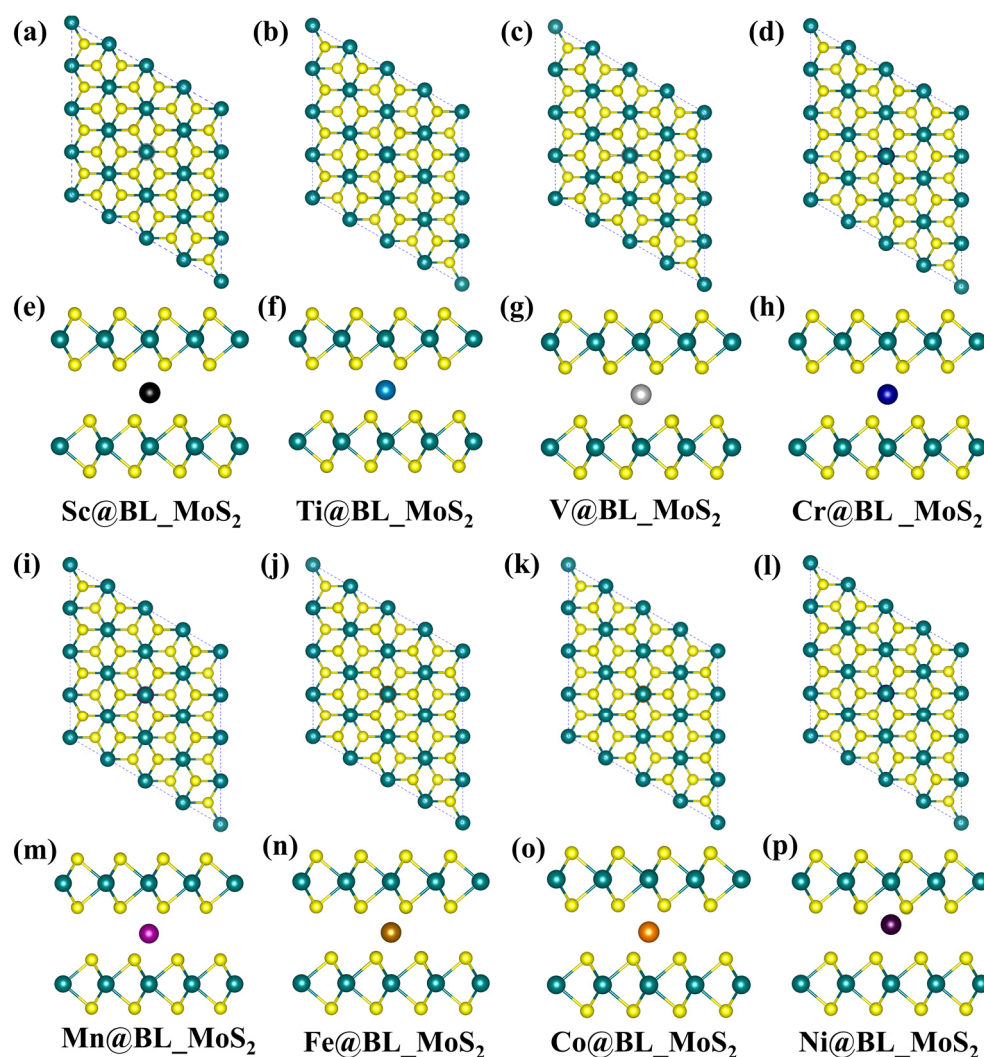


**Figure 2.** (a–d,i–l) Top views and (e–h,m–p) side views of the optimized structures for TM@BL\_MoS<sub>2</sub>s (TM = Sc–Ni).

**Table 1.** The interlayer spacing ( $d_{S-S}$ ), the distance between the TM atoms and the two-side MS<sub>2</sub> layer ( $d_{TM-S}$ ), magnetic moment ( $\mu$ ) per unit cell, binding energy ( $E_b$ ), the Bader charges transferred from TM to adjacent MS<sub>2</sub> layers ( $\Delta Q$ ), and ground state (GS) of TM@BL\_MS<sub>2</sub> systems.

Metal	$d_{S-S}/\text{Å}$	$d_{TM-S}/\text{Å}$	$\mu$ ( $\mu\text{B}$ )	$E_b$ (eV)	$\Delta Q$ ( $e^-$ )	GS
TM@BL_MoS <sub>2</sub>						
Sc	3.46	1.73	2.78	−6.50	1.48	M
Ti	3.34	1.67	2.45	−5.19	1.28	M
V	3.28	1.64	3.44	−6.80	1.10	HM
Cr	3.37	1.69	5.93	−5.66	0.92	HM
Mn	3.37	1.68	5.00	−5.82	0.89	SC
Fe	3.17	1.58	2.29	−5.42	0.73	M
Co	3.19	1.60	2.92	−7.11	0.60	M
Ni	3.16	1.09	0	−7.21	0.32	SC

Table 1. Cont.

Metal	$d_{S-S}/\text{\AA}$	$d_{TM-S}/\text{\AA}$	$\mu$ ( $\mu\text{B}$ )	$E_b$ (eV)	$\Delta Q$ ( $e^-$ )	GS
TM@BL_VS <sub>2</sub>						
Sc	3.37	1.69	36.86	−6.67	1.53	HM
Ti	3.31	1.66	37.65	−6.69	1.41	SC
V	3.16	1.58	38.94	−6.51	1.37	HM
Cr	3.03	1.51	33.79	−4.23	1.26	HM
Mn	3.05	1.52	40.62	−4.63	1.18	SC
Fe	3.09	1.55	39.71	−5.22	1.04	SC
Co	3.01	1.50	36.69	−5.78	0.65	SC
Ni	3.05	1.53	37.72	−5.45	0.61	SC

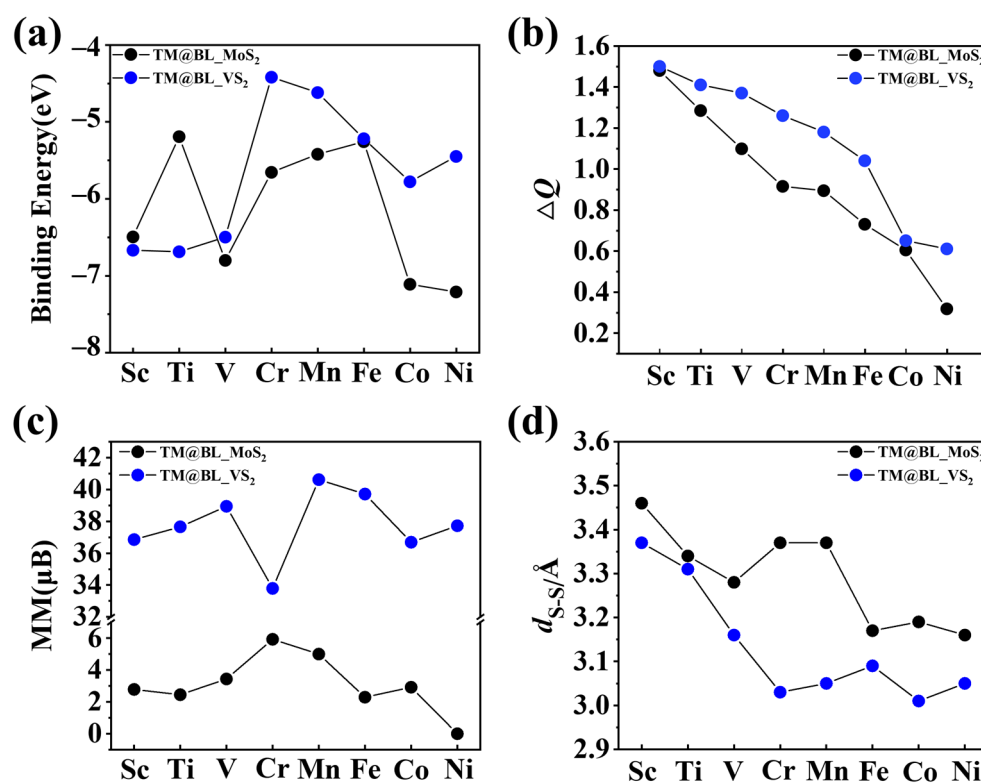


**Figure 3.** (a) The binding energy ( $E_b$ ) of TM-embedded MS<sub>2</sub> (M = Mo, V) bilayers. (b) The number of electrons transferred from TM atoms to adjacent MS<sub>2</sub> layers. (c) The magnetic moments (MM) and (d) the interlayer distance ( $d_{S-S}$ ) of TM@BL\_MS<sub>2</sub> systems.

In order to clarify the bonding characteristics of these systems, the charge density differences (CDDs) of TM@BL\_MS<sub>2</sub>s (TM = Ti, V, Cr) are given in Figure S3, which are calculated based on the following equation:

$$\Delta\rho = \rho_{[\text{TM@BL}_{\text{MS}_2}]} - \rho_{[\text{TM}]} - \rho_{[\text{MS}_2(\text{T})]} - \rho_{[\text{MS}_2(\text{L})]} \quad (2)$$

where  $\rho_{[\text{TM@BL}_{\text{MS}_2}]}$ ,  $\rho_{[\text{TM}]}$ ,  $\rho_{[\text{MS}_2(\text{T})]}$ ,  $\rho_{[\text{MS}_2(\text{L})]}$  represent the charge density of the whole system, the TM atom, the top MS<sub>2</sub> layer, and the low MS<sub>2</sub> layer, respectively. Clearly, the embedding of TM atoms resulted in charge redistribution in the Mo(V)S<sub>2</sub> sublayers. It was found that the charge densities were reduced at the center of TM atoms and accumulated between the TM-S bonds, indicating the obvious covalent bonding characteristics in the systems. Quantitatively, the Bader charges of the TM atoms were calculated (see Table 1). It can be seen that the amount of charge transfer gradually decreased from Sc to Ni in both TM@BL\_MoS<sub>2</sub> and TM@BL\_VS<sub>2</sub> systems (see Figure 3b). Moreover, the diffusion of Ti

atom in Ti@BL\_MoS<sub>2</sub> along the MoS<sub>2</sub> interface was examined (see Figure S4), and the large diffusion barrier (1.4 eV) confirms the difficulty of clustering of Ti atoms.

## 2.2. Electronic and Magnetic Properties of TM@BL\_MS<sub>2</sub> (TM = Sc–Ni, M = Mo, V)

The total magnetic moments of both TM@BL\_MoS<sub>2</sub>s and TM@BL\_VS<sub>2</sub>s are summarized in Table 1 and Figure 3c. Interestingly, the intercalation of TM atoms in MoS<sub>2</sub> bilayers introduces magnetism into the systems. Except for Ni@BL\_MoS<sub>2</sub>, all the other TM@BL\_MoS<sub>2</sub>s (TM = Sc–Co) exhibit ferromagnetism. Among them, Cr@BL\_MoS<sub>2</sub> has the largest magnetic moment (5.93  $\mu$ B), and Fe@BL\_MoS<sub>2</sub> displays the smallest one (2.29  $\mu$ B) per unit cell (see Table 1). Such induced ferromagnetisms in nonmagnetic MoS<sub>2</sub> bilayers are similar to those of TM-intercalated TMDs [27] and other 2D materials [28,48]. The partial density of states (PDOS) and spin density plots are shown in Figure 4. The magnetic moments of these TM@BL\_MoS<sub>2</sub> systems are mainly contributed by the 3d electrons from TM atoms. In addition, spin polarization of some Mo atoms close to the TM atoms occurs, as shown in the spin density plots in Figure 4. Taking Cr@BL\_MoS<sub>2</sub> as an example, five d orbitals ( $d_{xy}$ ,  $d_{x^2-y^2}$ ,  $d_{xz}$ ,  $d_{yz}$ ,  $d_{z^2}$ ) from the spin-up channel of the Cr atom contribute 5.0  $\mu$ B magnetic moment, and one d orbital from the spin-up channel of the two Mo atoms above/below the Cr atom contributes 1.0  $\mu$ B magnetic moment. As a result, the total magnetic moment of this system is about 6.0  $\mu$ B. Similar analysis can also be applied to other systems.

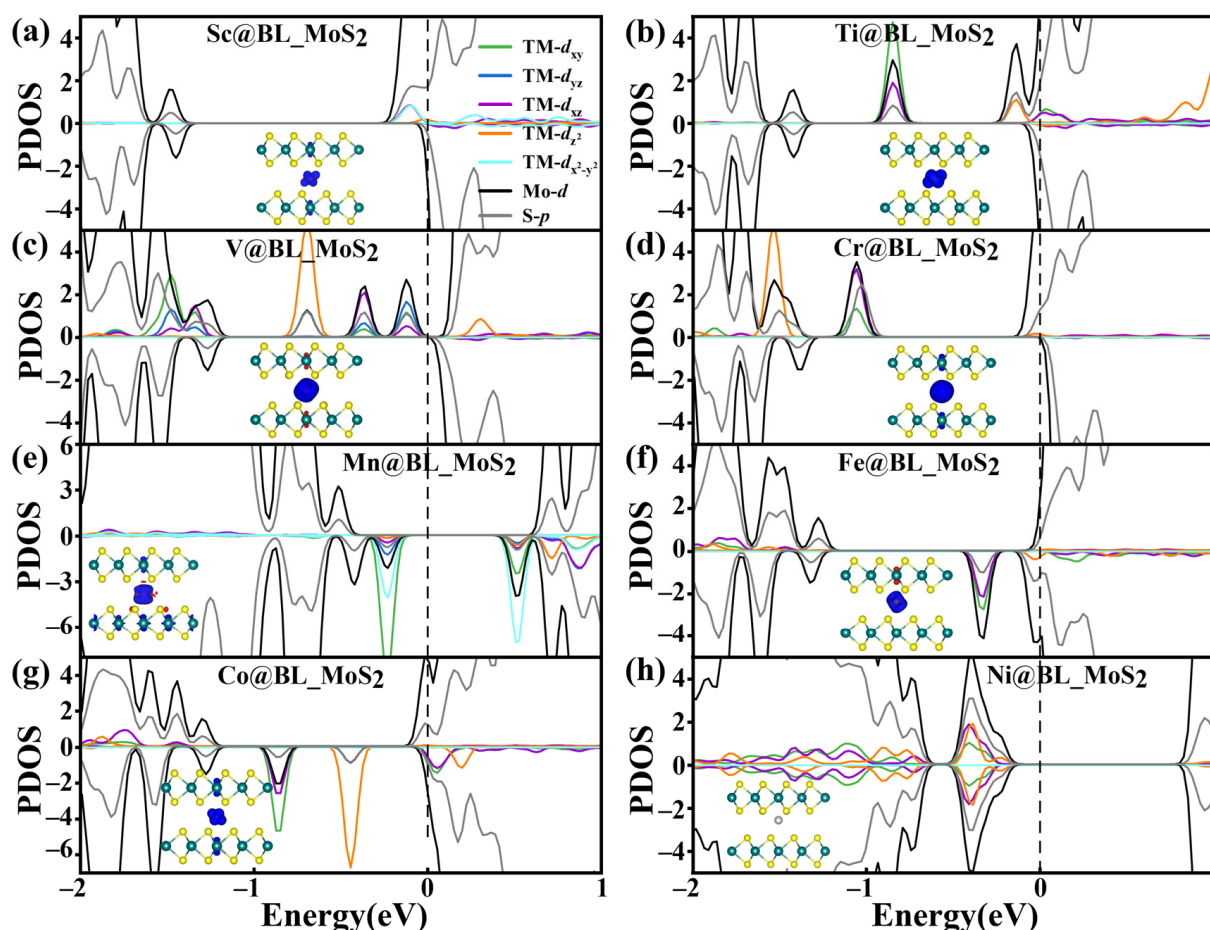


**Figure 4.** (a–h) Partial density of states (PDOS) and spin density plots for TM@BL\_MoS<sub>2</sub> (TM = Sc–Ni). Inside the PDOS graph is its corresponding spin density graph; blue represents positive spin, and red represents negative spin.

As for TM@BL\_VS<sub>2</sub>s, most systems are found to be ferromagnetic, with ferromagnetic coupling between V atoms and intercalated TM atoms (see Figure S5). The magnetic moments range from 36.69  $\mu\text{B}$  to 40.62  $\mu\text{B}$  per unit cell. Among them, Co@BL\_VS<sub>2</sub> has the smallest magnetic moment (36.69  $\mu\text{B}$ ), and Mn@BL\_VS<sub>2</sub> has the largest magnetic moment (40.62  $\mu\text{B}$ ). Exceptions are found for Sc@BL\_VS<sub>2</sub> and Cr@BL\_VS<sub>2</sub>. For the former, zero magnetic moment is found for the Sc atom, and for the latter, it is ferromagnetic, with the Cr atom displaying opposite magnetic moments to those of the V atoms.

Compared with the semiconducting properties of free-standing MoS<sub>2</sub> monolayers, TM@BL\_MoS<sub>2</sub>s (TM = Sc, Ti, Fe, Co) are changed to be ferromagnetic metals (see Figure 4 and Figure S6 and Table 1), in which the conduction band bottom passes through the Fermi level. V@BL\_MoS<sub>2</sub> and Cr@BL\_MoS<sub>2</sub> are ferromagnetic half-metals, in which one spin channel shows conducting behavior, and the contrast spin channel shows semiconducting properties. Besides, Mn@BL\_MoS<sub>2</sub> and Ni@BL\_MoS<sub>2</sub> are ferromagnetic semiconductor and non-magnetic semiconductor with band gaps of about 0.74 eV and 0.99 eV, respectively, which are significantly reduced compared to those of the MoS<sub>2</sub> monolayer (1.8 eV) [41]. Moreover, the embedded TM atom produces impurity energy bands in the gap of MoS<sub>2</sub>, leading to the Fermi level of the energy band shifting upwards moderately. For TM@BL\_VS<sub>2</sub>s, as shown in Figure S7, the systems with TM = Sc, V, Cr become ferromagnetic or ferrimagnetic half-metals. In the case of TM@BL\_VS<sub>2</sub>s with TM = Ti, Mn, Fe, Co, Ni, they are all ferromagnetic semiconductors with a band gap of about 0.52, 0.46, 0.53, 0.19, and 0.52 eV, respectively.

### 2.3. Effect of TM Intercalation Concentration on the TM BL\_MS<sub>2</sub> (TM = V, Cr, Mn, Fe, M = Mo)

In order to determine the influence of TM intercalation ratios on the structures and electronic properties of these systems, the structures intercalated with two or more TM atoms (TM = V, Cr, Mn, Fe), i.e., 2TM@BL\_MoS<sub>2</sub> and TMC@BL\_MoS<sub>2</sub>, were considered, in which two adjacent TM atoms inserted in the 4  $\times$  4 supercell and one chain intercalated TM atoms inserted in the 4  $\times$  1 supercell were considered. The optimized structures of 2TM@BL\_MoS<sub>2</sub>s and TMC@BL\_MoS<sub>2</sub>s are shown in Figure 5. Similar to the TM@BL\_MoS<sub>2</sub> systems, the TM atoms from the 2TM@BL\_MoS<sub>2</sub> and TMC@BL\_MoS<sub>2</sub> systems were firmly stabilized in the middle of the space of the MoS<sub>2</sub> bilayer. Moreover, for the 2TM@BL\_MoS<sub>2</sub> systems, the interlayer distances were around 3.44 Å, 3.55 Å, 3.50 Å, and 3.24 Å, and the distances between TM atoms and the two-side MoS<sub>2</sub> layer were 1.72 Å, 1.77 Å, 1.75 Å, and 1.62 Å in the systems with TM = V, Cr, Mn, Fe, respectively (see Table 2). As for TMC@BL\_MoS<sub>2</sub>s, the interlayer distances were around 3.14 Å, 4.56 Å, 3.43 Å, and 3.54 Å for the structures inserted with chains of V, Cr, Mn, and Fe, respectively, and the distances between TM atoms and adjacent MoS<sub>2</sub> layers were around 1.57 Å, 2.27 Å, 1.71 Å, and 1.77 Å, respectively (see Table 2). The binding energies of these 2TM@BL\_MoS<sub>2</sub> and TMC@BL\_MoS<sub>2</sub> systems were in the range of  $-4.21\sim-3.45$  eV and  $-3.39\sim-1.95$  eV, respectively, in which the systems with Mn atoms exhibited the lowest  $E_{\text{bs}}$ , while those with the V atoms showed the largest  $E_{\text{bs}}$ . Similar to those TM@BL\_MoS<sub>2</sub> systems, the charges transferred from TM to adjacent MoS<sub>2</sub> layers per unit cell were in the range of 0.73~1.13 $e$  and 0.73~1.09 $e$  for the 2TM@BL\_MoS<sub>2</sub> and TMC@BL\_MoS<sub>2</sub> systems, respectively (see Figure S8 and Table 2).

The PDOS, spin density diagram, and band structures of these 2TM@BL\_MoS<sub>2</sub>s and TMC@BL\_MoS<sub>2</sub>s are shown in Figure 6 and Figure S9. It was found that all 2TM@BL\_MoS<sub>2</sub>s and TMC@BL\_MoS<sub>2</sub>s are FM metals except for 2V@BL\_MoS<sub>2</sub>, which is FM half-metal. For 2TM@BL\_MoS<sub>2</sub>s, the magnetic moments were 7.85  $\mu\text{B}$ , 11.89  $\mu\text{B}$ , 10  $\mu\text{B}$ , and 6.14  $\mu\text{B}$  per unit cell for the systems with TM = V, Cr, Mn, Fe, respectively, nearly double those of their TM@BL\_MoS<sub>2</sub> counterparts (see Table 2). As for TMC@BL\_MoS<sub>2</sub>s, the magnetic moments were 3.03  $\mu\text{B}$ , 5.17  $\mu\text{B}$ , 3.61  $\mu\text{B}$ , and 2.44  $\mu\text{B}$  per unit cell for the ones with TM = V, Cr, Mn, Fe, respectively. Similar to TM@BL\_MoS<sub>2</sub>s, the magnetic moments of the above systems were mainly contributed by the inserted 3d TM atoms (see Figure 6). However, the magnetic moments per unit cell of TMC@BL\_MoS<sub>2</sub>s differed from those of TM@BL\_MoS<sub>2</sub>s,

indicating that the magnetic properties of these systems are sensitive to the intercalated TM concentrations. Moreover, with the intercalated TM atom increasing, the electronic states around the Fermi level increased, leading to the metallic character in them. Specifically, the number of impurity bands from TM atoms in 2TM@BL\_MoS<sub>2</sub>s increased and almost doubled those in TM@BL\_MoS<sub>2</sub>s (see Figure S9). In contrast, in TMC@BL\_MoS<sub>2</sub>s, the electronic bands around the Fermi level were no longer flat and became much more dispersed, indicating that the hybridization between TM<sub>d</sub> and MoS<sub>2</sub><sub>p</sub> orbitals was largely strengthened. Therefore, it is very effective to control the electronic and magnetic properties of these systems by varying the TM ratios.

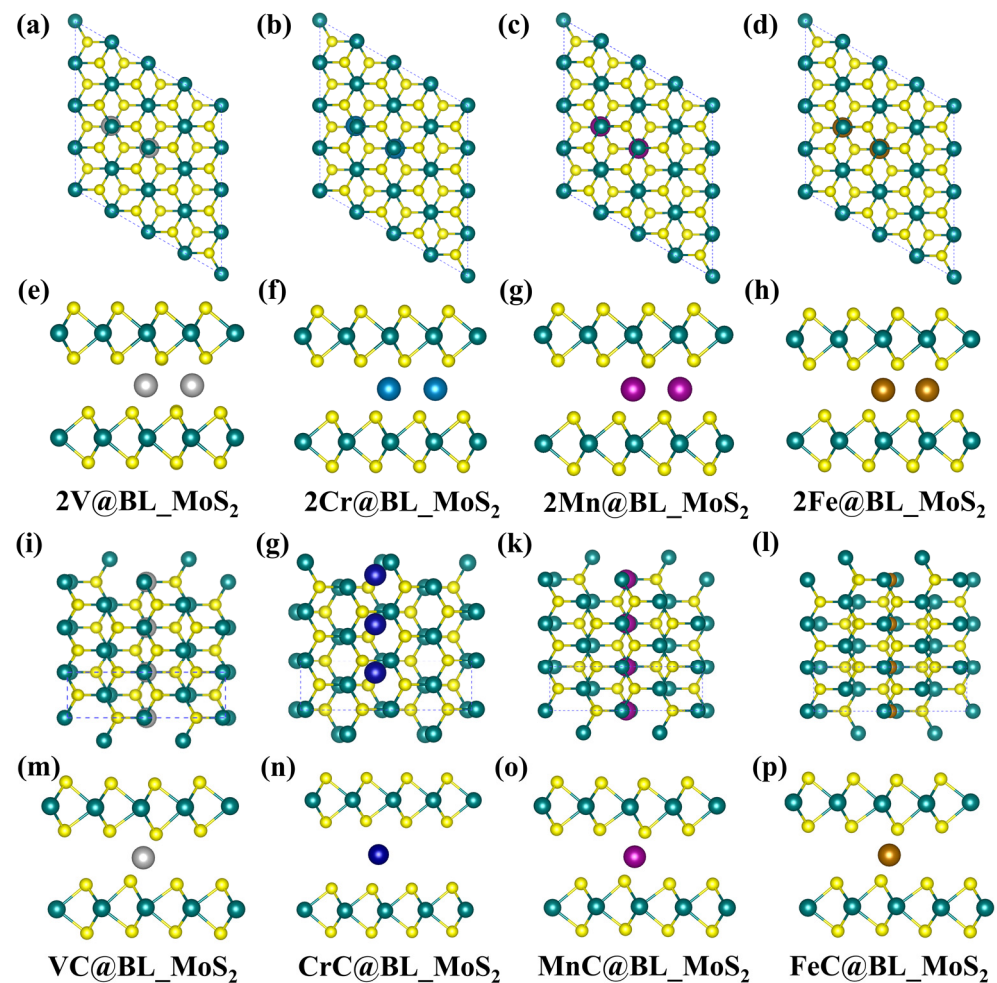


**Figure 5.** (a–d,i–l) Top views and (e–h,m–p) side views of the optimized structure of 2TM@BL\_MoS<sub>2</sub>s and TMC@BL\_MoS<sub>2</sub>s (TM = V, Cr, Mn, Fe), respectively.

**Table 2.** The interlayer spacing ( $d_{S-S}$ ), the distance between the TM atoms and the two-side MoS<sub>2</sub> layer ( $d_{TM-S}$ ), magnetic moment ( $\mu$ ) per unit cell, binding energy ( $E_b$ ) per TM atom, the Bader charges transferred from TM to adjacent MoS<sub>2</sub> layers ( $\Delta Q$ ), and ground states (GS) of 2TM@BL\_MoS<sub>2</sub>s and TMC@BL\_MoS<sub>2</sub>s.

Metal	$d_{S-S}/\text{\AA}$	$d_{TM-S}/\text{\AA}$	$\mu$ ( $\mu_B$ )	$E_b$ (eV)	$\Delta Q$ ( $e^-$ )	GS
2TM@BL_MoS <sub>2</sub>						
2V	3.44	1.72	7.85	−4.21	1.13	HM
2Cr	3.55	1.77	11.89	−3.79	0.98	M
2Mn	3.50	1.75	10.00	−3.45	0.95	M
2Fe	3.23	1.62	6.14	−4.18	0.73	M



Table 2. Cont.

Metal	$d_{S-S}/\text{\AA}$	$d_{TM-S}/\text{\AA}$	$\mu$ ( $\mu\text{B}$ )	$E_b$ (eV)	$\Delta Q$ ( $e^-$ )	GS
TMC@BL_MoS <sub>2</sub>						
VC	3.14	1.57	3.03	−3.39	1.09	M
CrC	4.55	2.27	5.14	−2.35	0.64	M
MnC	3.43	1.71	3.61	−1.95	0.95	M
FeC	3.54	1.77	2.44	−3.04	M	

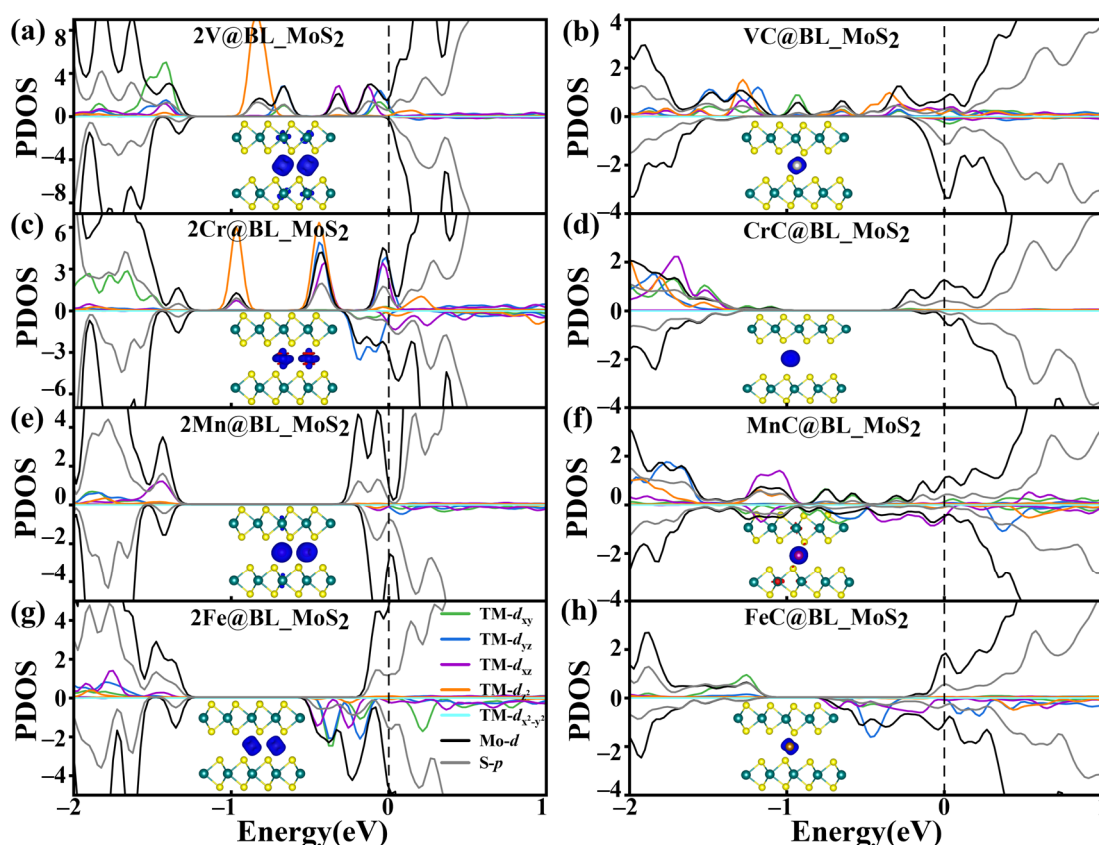


**Figure 6.** (a–d) Partial density of states (PDOS) and spin density plots for 2TM@BL\_MoS<sub>2</sub> (TM = V, Cr, Mn, Fe). (e–h) Partial density of states (PDOS) and spin density plots for TMC@BL\_MoS<sub>2</sub> (TM = V, Cr, Mn, Fe). Inside the PDOS graph is its corresponding spin density graph; blue represents positive spin, and red represents negative spin.

### 3. Methods

All the calculations were performed using the Vienna ab initio simulation package (VASP) [49–51]. The exchange–correlation potentials were treated by the generalized gradient approximation (GGA) of optimized Perdew–Burke–Ernzerhof (PBE) [52]. The interactions between the ion core and the valence electrons were modeled with projector augmented wave (PAW) potentials [53], and the DFT-D2 method was used to account for van der Waals (vdW) interaction [54]. A vacuum layer of 20 Å was added in the z direction to eliminate the interaction of interlayer caused by periodic boundary conditions. In order to consider the Coulomb interaction and exchange interactions on TM electrons, the GGA+U method with  $U_{eff} = 4.0$  eV was adopted according to the previous literature, which has been proven to give very close results for these systems [55–58]. A plane-wave basis set with a kinetic cutoff energy of 500 eV was employed. The  $4 \times 4$  supercells with the lattice constants of  $a = b = 12.76$  Å and  $a = b = 12.72$  Å for bilayer MoS<sub>2</sub> and VS<sub>2</sub> were applied, respectively. The Brillouin zone (BZ) was sampled using  $3 \times 3 \times 1$  and  $5 \times 5 \times 1$  gamma-centered Monkhorst–Pack grids for the calculation of structural relaxation and electronic structures,

respectively. The criteria for energy and atomic force convergence were set to  $10^{-5}$  eV per unit cell and  $0.01$  eV  $\text{\AA}^{-1}$ , respectively.

#### 4. Conclusions

In summary, the structural, electronic, and magnetic properties of 3d TM atom (TM = Ti–Ni)-intercalated Mo(V)S<sub>2</sub> bilayers, TM@BL\_Mo(V)S<sub>2</sub>, are explored using density functional theory methods. All the studied systems are thermal dynamically stable with large binding energies, ranging from  $-4.23$  to  $-7.21$  eV. The intercalation of TM atoms introduces rich electronic and magnetic properties to Mo(V)S<sub>2</sub> bilayers. Except for Ni@BL\_MoS<sub>2</sub>, which is a nonmagnetic semiconductor, most studied systems are found to display robust magnetic properties. TM@BL\_MoS<sub>2</sub>s (TM = Sc, Ti, Fe, Co) are ferromagnetic metals, TM@BL\_MoS<sub>2</sub> (TM = V, Cr) and TM@BL\_VS<sub>2</sub> (TM = Sc, V, Cr) are ferromagnetic or ferrimagnetic half-metals, and the remaining systems are found to be ferromagnetic semiconductors. Furthermore, the electronic and magnetic properties of these TM@BL\_MoS<sub>2</sub>s are largely influenced by the concentration of TM atoms. Our study proposes that the intercalation of TM atoms is a feasible way to tune the properties of 2D materials and promote their potential applications in electronic and spin electronic devices.

**Supplementary Materials:** The following supporting information can be downloaded at <https://www.mdpi.com/article/10.3390/inorganics12090237/s1>; Figure S1: Top and side views of AA-, AB-, and AB'-stacking of bilayer VS<sub>2</sub> and TM@BL\_VS<sub>2</sub>, with TM intercalating at the A site and B site; Figure S2: Top and side views of the optimized structures for TM@BL\_VS<sub>2</sub>s; Figure S3: The CDDs plots of TM@BL\_MoS<sub>2</sub> (TM = Ti, V, Cr) and TM@BL\_VS<sub>2</sub> (TM = Ti, V, Cr); Figure S4: Energy barrier for Ti@BL\_MoS<sub>2</sub> diffusion from position A to position B; Figure S5: Partial density of states (PDOS) and spin density plots for TM@BL\_VS<sub>2</sub>s; Figure S6: Band structures of TM@BL\_MoS<sub>2</sub>s; Figure S7: Band structures of TM@BL\_VS<sub>2</sub>s; Figure S8: The CDDs plots of 2TM@BL\_MoS<sub>2</sub> (TM = V, Cr, Mn, Fe) and TMC@BL\_MoS<sub>2</sub> (TM = V, Cr, Mn, Fe); Figure S9: Band structures of 2TM@BL\_MoS<sub>2</sub> (TM = V, Cr, Mn, Fe) and TMC@BL\_MoS<sub>2</sub> (TM = V, Cr, Mn, Fe).

**Author Contributions:** Conceptualization, Y.L. (Yujie Liu) and X.Z.; data curation, Y.L. (Yujie Liu) and G.Y.; formal analysis, Y.L. (Yujie Liu), G.Y., Z.H. and Y.W.; investigation, G.Y., Z.H. and X.Z.; writing—original draft, Y.L. (Yujie Liu) and G.Y.; writing—review and editing, Y.L. (Yujie Liu), Y.W., Y.L. (Yongjun Liu) and X.Z.; supervision, Y.W., X.N., S.W. and X.Z.; project administration, Y.L. (Yongjun Liu), X.N. and S.W. All authors have read and agreed to the published version of the manuscript.

**Funding:** This research was funded by the Six Talent Peaks Project in Jiangsu Province (XCL-104), the Natural Science Foundation of Jiangsu Province (No. BK20211002), as well as Qinglan Project of Jiangsu Province of China. China Postdoctoral Science Foundation (No. 2022M711691), National Natural Science Foundation of China (No. 22473060).

**Data Availability Statement:** Data are included within the article and Supplementary Materials.

**Acknowledgments:** We thank the computational resources at Yangzhou University.

**Conflicts of Interest:** The authors declare no conflicts of interest.

#### References

1. Geim, A.K.; Novoselov, K.S. The rise of graphene. *Nat. Mater.* **2007**, *6*, 183–191. [[CrossRef](#)] [[PubMed](#)]
2. Novoselov, K.S.; Geim, A.K.; Morozov, S.V.; Jiang, D.; Zhang, Y.; Dubonos, S.V.; Grigorieva, I.V.; Firsov, A.A. Electric field effect in atomically thin carbon films. *Science* **2004**, *306*, 666–669. [[CrossRef](#)]
3. Wang, Q.H.; Kalantar-Zadeh, K.; Kis, A.; Coleman, J.N.; Strano, M.S. Electronics and optoelectronics of two-dimensional transition metal dichalcogenides. *Nat. Nanotechnol.* **2012**, *7*, 699–712. [[CrossRef](#)]
4. Chen, S.; Shi, G.Q. Two-dimensional materials for halide perovskite-based optoelectronic devices. *Adv. Mater.* **2017**, *29*, 1605448. [[CrossRef](#)]
5. Geim, A.K.; Grigorieva, I.V. Van der Waals heterostructures. *Nature* **2013**, *499*, 419–425. [[CrossRef](#)]
6. Williams, T.J.; Aczel, A.A.; Lumsden, M.D.; Nagler, S.E.; Stone, M.B.; Yan, J.Q.; Mandrus, D. Magnetic correlations in the quasi-two-dimensional semiconducting ferromagnet CrSiTe<sub>3</sub>. *Phys. Rev. B* **2015**, *92*, 144404. [[CrossRef](#)]
7. Jiang, S.W.; Li, L.Z.; Wang, Z.F.; Mak, K.F.; Shan, J. Controlling magnetism in 2D CrI<sub>3</sub> by electrostatic doping. *Nat. Nanotechnol.* **2018**, *13*, 549–553. [[CrossRef](#)]

8. Son, S.; Coak, M.J.; Lee, N.; Kim, J.; Kim, T.Y.; Hamidov, H.; Cho, H.; Liu, C.; Jarvis, D.M.; Brown, P.A.C.; et al. Bulk properties of the van der Waals hard ferromagnet  $\text{Vl}_3$ . *Phys. Rev. B* **2019**, *99*, 041402. [[CrossRef](#)]
9. Gong, C.; Li, L.; Li, Z.L.; Ji, H.W.; Stern, A.; Xia, Y.; Cao, T.; Bao, W.; Wang, C.Z.; Wang, Y.A.; et al. Discovery of intrinsic ferromagnetism in two-dimensional van der Waals crystals. *Nature* **2017**, *546*, 265–269. [[CrossRef](#)]
10. Meng, L.J.; Zhou, Z.; Xu, M.Q.; Yang, S.Q.; Si, K.P.; Liu, L.X.; Wang, X.G.; Jiang, H.N.; Li, B.X.; Qin, P.X.; et al. Anomalous thickness dependence of Curie temperature in air-stable two-dimensional ferromagnetic  $1\text{T-CrTe}_2$  grown by chemical vapor deposition. *Nat. Commun.* **2021**, *12*, 809. [[CrossRef](#)]
11. Qin, J.; Yang, C.; Yakushi, K.; Nakazawa, Y.; Ichimura, K.; Liu, D. Synthesis and ferromagnetism of a new intercalation compound:  $\text{Mn}_{0.86}\text{PS}_3(\text{bipy})_{0.56}$ . *Synth. Met.* **1997**, *85*, 1673–1674. [[CrossRef](#)]
12. Chu, H.; Roh, C.J.; Island, J.O.; Li, C.; Lee, S.; Chen, J.J.; Park, J.G.; Young, A.F.; Lee, J.S.; Hsieh, D. Linear magnetoelectric phase in ultrathin  $\text{MnPS}_3$  probed by optical second harmonic generation. *Phys. Rev. Lett.* **2020**, *124*, 027601. [[CrossRef](#)] [[PubMed](#)]
13. Chittari, B.L.; Park, Y.; Lee, D.; Han, M.; MacDonald, A.H.; Hwang, E.; Jung, J. Electronic and magnetic properties of single-layer  $\text{MPX}_3$  metal phosphorous trichalcogenides. *Phys. Rev. B* **2016**, *94*, 184428. [[CrossRef](#)]
14. Li, Q.; Zhou, D.; Zheng, W.; Ma, Y.; Chen, C. Global structural optimization of tungsten borides. *Phys. Rev. Lett.* **2013**, *110*, 136403. [[CrossRef](#)]
15. Sharma, A.; Rangra, V.S.; Thakur, A. Synthesis, properties, and applications of MBenes (two-dimensional metal borides) as emerging 2D materials: A review. *J. Mater. Sci.* **2022**, *57*, 12738–12751. [[CrossRef](#)]
16. Zhang, B.; Zhou, J.; Sun, Z. MBenes: Progress, challenges and future. *J. Mater. Chem. A* **2022**, *10*, 15865–15880. [[CrossRef](#)]
17. Du, M.; Li, D.; Liu, S.; Yan, J. Transition metal phosphides: A wonder catalyst for electrocatalytic hydrogen production. *Chin. Chem. Lett.* **2023**, *34*, 108156. [[CrossRef](#)]
18. Zhang, N.; Amorim, I.; Liu, L. Multimetallic transition metal phosphide nanostructures for supercapacitors and electrochemical water splitting. *Nanotechnology* **2022**, *33*, 432004. [[CrossRef](#)]
19. Yang, Y.; Zhou, C.; Wang, W.; Xiong, W.; Zeng, G.; Huang, D.; Zhang, C.; Song, B.; Xue, W.; Li, X.; et al. Recent advances in application of transition metal phosphides for photocatalytic hydrogen production. *Chem. Eng. J.* **2021**, *405*, 126547. [[CrossRef](#)]
20. Sun, L.; Leong, W.S.; Yang, S.; Chisholm, M.F.; Liang, S.-J.; Ang, L.K.; Tang, Y.; Mao, Y.; Kong, J.; Yang, H.Y. Concurrent synthesis of high-performance monolayer transition metal disulfides. *Adv. Funct. Mater.* **2017**, *27*, 1605896. [[CrossRef](#)]
21. Cheng, J.; Jin, Y.; Zhao, J.; Jing, Q.; Gu, B.; Wei, J.; Yi, S.; Li, M.; Nie, W.; Qin, Q.; et al. From VIB- to VB-group transition metal disulfides: Structure engineering modulation for superior electromagnetic wave absorption. *Nano-Micro Lett.* **2023**, *16*, 29. [[CrossRef](#)] [[PubMed](#)]
22. Liu, H.; Qi, G.; Tang, C.; Chen, M.; Chen, Y.; Shu, Z.; Xiang, H.; Jin, Y.; Wang, S.; Li, H.; et al. Growth of large-area homogeneous monolayer transition-metal disulfides via a molten liquid intermediate process. *ACS Appl. Mater.* **2020**, *12*, 13174–13181. [[CrossRef](#)] [[PubMed](#)]
23. Zhao, C.Y.; Jin, C.H.; Wu, J.L.; Ji, W. Magnetism in molybdenum disulphide monolayer with sulfur substituted by  $3d$  transition metals. *J. Appl. Phys.* **2016**, *120*, 144305. [[CrossRef](#)]
24. Lopez-Bezanilla, A.; Lado, J.L. Defect-induced magnetism and Yu-Shiba-Rusinov states in twisted bilayer graphene. *Phys. Rev. Mater.* **2019**, *3*, 084003. [[CrossRef](#)]
25. Zhang, X.Y.; Xi, B.; Liu, Y.J.; Yao, X.J.; Wu, X.J. Antiferromagnetic semimetal in Ti-intercalated borophene heterobilayer. *J. Phys. Chem. C* **2020**, *124*, 4709–4716. [[CrossRef](#)]
26. Wan, J.Y.; Lacey, S.D.; Dai, J.Q.; Bao, W.Z.; Fuhrer, M.S.; Hu, L.B. Tuning two-dimensional nanomaterials by intercalation: Materials, properties and applications. *Chem. Soc. Rev.* **2016**, *45*, 6742–6765. [[CrossRef](#)]
27. Kumar, P.; Skomski, R.; Pushpa, R. Magnetically ordered transition-metal-intercalated  $\text{WSe}_2$ . *ACS Omega* **2017**, *2*, 7985–7990. [[CrossRef](#)]
28. Zhang, X.Y.; Xu, W.X.; Dai, J.P.; Liu, Y.J. Role of embedded  $3d$  transition metal atoms on the electronic and magnetic properties of defective bilayer graphene. *Carbon* **2017**, *118*, 376–383. [[CrossRef](#)]
29. Chen, Z.; Leng, K.; Zhao, X.; Malkhandi, S.; Tang, W.; Tian, B.; Dong, L.; Zheng, L.; Lin, M.; Yeo, B.S.; et al. Interface confined hydrogen evolution reaction in zero valent metal nanoparticles-intercalated molybdenum disulfide. *Nat. Commun.* **2017**, *8*, 14548. [[CrossRef](#)]
30. Zhang, M.; Zhang, C.; You, Y.; Xie, H.; Chi, H.; Sun, Y.; Liu, W.; Su, X.; Yan, Y.; Tang, X.; et al. Electron density optimization and the anisotropic thermoelectric properties of Ti self-intercalated  $\text{Ti}_{1+x}\text{S}_2$  compounds. *ACS Appl. Mater.* **2018**, *10*, 32344–32354. [[CrossRef](#)]
31. Li, F.; Hu, R.; Huang, Z.; Luo, S.; Qiao, H.; Zhong, J.; Qi, X. Properties tuning and applications for two dimension materials in electrochemical intercalation process. *Appl. Mater. Today* **2024**, *36*, 102069. [[CrossRef](#)]
32. Rajapakse, M.; Karki, B.; Abu, U.O.; Pishgar, S.; Musa, M.R.K.; Riyadh, S.M.S.; Yu, M.; Sumanasekera, G.; Jasinski, J.B. Intercalation as a versatile tool for fabrication, property tuning, and phase transitions in 2D materials. *NPJ 2D Mater. Appl.* **2021**, *5*, 30. [[CrossRef](#)]
33. Guzman, R.; Liu, H.; Bian, C.; Bao, L.; Shen, C.-M.; Gao, H.-J.; Zhou, W. Temperature-induced structural evolution and magnetism in self-intercalated  $\text{V}_{1+x}\text{Se}_2$  nanoplates. *Adv. Funct. Mater.* **2024**, 2401304. [[CrossRef](#)]
34. Zhao, X.X.; Song, P.; Wang, C.C.; Riis-Jensen, A.C.; Fu, W.; Deng, Y.; Wan, D.Y.; Kang, L.X.; Ning, S.C.; Dan, J.D.; et al. Engineering covalently bonded 2D layered materials by self-intercalation. *Nature* **2020**, *581*, 171–177. [[CrossRef](#)]

35. Niu, J.; Yan, B.; Ji, Q.; Liu, Z.; Li, M.; Gao, P.; Zhang, Y.; Yu, D.; Wu, X. Anomalous hall effect and magnetic orderings in nanothick  $V_5S_8$ . *Phys. Rev. B* **2017**, *96*, 075402. [[CrossRef](#)]
36. Matsuoka, H.; Barnes, S.E.; Ieda, J.I.; Maekawa, S.; Bahramy, M.S.; Saika, B.K.; Takeda, Y.; Wadati, H.; Wang, Y.; Yoshida, S.; et al. Spin-orbit-induced ising ferromagnetism at a van der Waals interface. *Nano Lett.* **2021**, *21*, 1807–1814. [[CrossRef](#)] [[PubMed](#)]
37. Fujisawa, Y.; Pardo-Almanza, M.; Garland, J.; Yamagami, K.; Zhu, X.; Chen, X.; Araki, K.; Takeda, T.; Kobayashi, M.; Takeda, Y.; et al. Tailoring magnetism in self-intercalated  $Cr_{1+\delta}Te_2$  epitaxial films. *Phys. Rev. Mater.* **2020**, *4*, 114001. [[CrossRef](#)]
38. Saha, R.; Meyerheim, H.L.; Göbel, B.; Hazra, B.K.; Deniz, H.; Mohseni, K.; Antonov, V.; Ernst, A.; Knyazev, D.; Bedoya-Pinto, A.; et al. Observation of Neel-type skyrmions in acentric self-intercalated  $Cr_{1+\delta}Te_2$ . *Nat. Commun.* **2022**, *13*, 3965. [[CrossRef](#)]
39. Guo, Y.; Liu, N.; Zhao, Y.; Jiang, X.; Zhou, S.; Zhao, J. Enhanced ferromagnetism of  $CrI_3$  bilayer by self-intercalation. *Chin. Phys. Lett.* **2020**, *37*, 107506. [[CrossRef](#)]
40. Tan, F.; Li, J.; Fang, X.; Guan, L. The optical properties of few-layer  $MoS_2$  by DFT calculations. *Phys. E* **2024**, *155*, 115813. [[CrossRef](#)]
41. Mak, K.F.; Lee, C.; Hone, J.; Shan, J.; Heinz, T.F. Atomically thin  $MoS_2$ : A new direct-gap semiconductor. *Phys. Rev. Lett.* **2010**, *105*, 136805. [[CrossRef](#)] [[PubMed](#)]
42. Szary, M.J. Adsorption of ethylene oxide on doped monolayers of  $MoS_2$ : A DFT study. *Mater. Sci. Eng. B* **2021**, *265*, 115009. [[CrossRef](#)]
43. Dai, J.-Q.; Yuan, J.; Ke, C. Synergistic magnetic proximity and ferroelectric field effect on a 2H- $VS_2$  monolayer by ferromagnetic termination of a  $BiFeO_3(0001)$  surface. *J. Mater. Chem. C* **2022**, *10*, 1498–1510. [[CrossRef](#)]
44. Kan, M.; Wang, B.; Lee, Y.H.; Sun, Q. A density functional theory study of the tunable structure, magnetism and metal-insulator phase transition in  $VS_2$  monolayers induced by in-plane biaxial strain. *Nano Res.* **2015**, *8*, 1348–1356. [[CrossRef](#)]
45. Karthick, K.; Bijoy, T.K.; Sivakumaran, A.; Mansoor Basha, A.B.; Murugan, P.; Kundu, S. Enhancing hydrogen evolution reaction activities of 2H-phase  $VS_2$  layers with palladium nanoparticles. *Inorg. Chem.* **2020**, *59*, 10197–10207. [[CrossRef](#)] [[PubMed](#)]
46. Cui, Y.; Fan, W.; Liu, X.; Ren, J.; Gao, Y. Electronic conductivity of two-dimensional  $VS_2$  monolayers: A first principles study. *Comp. Mater. Sci.* **2021**, *200*, 110767. [[CrossRef](#)]
47. Liu, X.; Pyatakov, A.P.; Ren, W. Magnetoelectric coupling in multiferroic bilayer  $VS_2$ . *Phys. Rev. Lett.* **2020**, *125*, 247601. [[CrossRef](#)] [[PubMed](#)]
48. Zhang, X.; Sun, Y.; Gao, W.; Lin, Y.; Zhao, X.; Wang, Q.; Yao, X.; He, M.; Ye, X.; Liu, Y. Sizable bandgaps of graphene in 3d transition metal intercalated defective graphene/ $WSe_2$  heterostructures. *RSC Adv.* **2019**, *9*, 18157–18164. [[CrossRef](#)] [[PubMed](#)]
49. Kresse, G.; Furthmüller, J. Efficient iterative schemes for ab initio total-energy calculations using a plane-wave basis set. *Phys. Rev. B* **1996**, *54*, 11169–11186. [[CrossRef](#)]
50. Kresse, G.; Hafner, J. Ab initio molecular dynamics for liquid metals. *Phys. Rev. B* **1993**, *47*, 558–561. [[CrossRef](#)]
51. Kresse, G.; Hafner, J. Ab initio molecular-dynamics simulation of the liquid-metal—Amorphous-semiconductor transition in germanium. *Phys. Rev. B* **1994**, *49*, 14251–14269. [[CrossRef](#)]
52. Perdew, J.P.; Burke, K.; Ernzerhof, M. Generalized gradient approximation made simple. *Phys. Rev. Lett.* **1996**, *77*, 3865–3868. [[CrossRef](#)] [[PubMed](#)]
53. Blöchl, P.E. Projector augmented-wave method. *Phys. Rev. B* **1994**, *50*, 17953–17979. [[CrossRef](#)] [[PubMed](#)]
54. Grimme, S. Semiempirical GGA-type density functional constructed with a long-range dispersion correction. *J. Comput. Chem.* **2006**, *27*, 1787–1799. [[CrossRef](#)]
55. Anasori, B.; Shi, C.; Moon, E.J.; Xie, Y.; Voigt, C.A.; Kent, P.R.C.; May, S.J.; Billinge, S.J.L.; Barsoum, M.W.; Gogotsi, Y. Control of electronic properties of 2D carbides (MXenes) by manipulating their transition metal layers. *Nanoscale Horiz.* **2016**, *1*, 227–234. [[CrossRef](#)]
56. Zhang, X.; Wei, J.; Li, R.; Zhang, C.; Zhang, H.; Han, P.; Fan, C. DFT + U predictions: Structural stability, electronic and optical properties, oxidation activity of  $BiOCl$  photocatalysts with 3d transition metals doping. *J. Mater. Sci.* **2018**, *53*, 4494–4506. [[CrossRef](#)]
57. Liu, C.; Fu, B.; Yin, H.; Zhang, G.; Dong, C. Strain-tunable magnetism and nodal loops in monolayer  $MnB$ . *Appl. Phys. Lett.* **2020**, *117*, 103101. [[CrossRef](#)]
58. Islam, M.F.; Canali, C.M.; Pertsova, A.; Balatsky, A.; Mahatha, S.K.; Carbone, C.; Barla, A.; Kokh, K.A.; Tereshchenko, O.E.; Jiménez, E.; et al. Systematics of electronic and magnetic properties in the transition metal doped  $Sb_2Te_3$  quantum anomalous hall platform. *Phys. Rev. B* **2018**, *97*, 155429. [[CrossRef](#)]

**Disclaimer/Publisher’s Note:** The statements, opinions and data contained in all publications are solely those of the individual author(s) and contributor(s) and not of MDPI and/or the editor(s). MDPI and/or the editor(s) disclaim responsibility for any injury to people or property resulting from any ideas, methods, instructions or products referred to in the content.